

Particle image velocimetry experiments on a macro-scale model for bacterial flagellar bundling

Min Jun Kim, Mun Ju Kim, James. C. Bird, Jinil Park, Thomas. R. Powers, Kenneth S. Breuer

782

Abstract *Escherichia coli* (*E. coli*) and other bacteria are propelled through water by several helical flagella, which are rotated by motors embedded at random points on the cell wall. Depending on the handedness and rotation sense, the motion of the flagella induces a flow field that causes them to wrap around each other and form a bundle. Our objective is to understand and model the mechanics of this process. Full-scale flagella are 10 μm in length, 20 nm in diameter, and turn at a rate of 100 Hz. To accurately simulate bundling at a more easily observable scale, we built a scale model in which 20-cm-long helices are rotated in 100,000 cp silicone oil (Poly-di-methyl-siloxane). The highly viscous oil ensures an appropriately low Reynolds number. We developed a macro-scale particle image velocimetry (PIV) system to measure the full-field velocity distribution for rotating rigid helices and rotating flexible helices. In the latter case, the helices were made from epoxy-filled plastic tubing to give approximately the same ratio of elastic to viscous stresses as in the full-scale flagella. Comparison between PIV measurements and slender-body calculations shows good agreement for the case of rigid helices. For the flexible helices, we find that the flow field generated by a bundle in the steady state is well approximated by the flow generated by a single rigid helix with twice the filament radius.

1 Introduction

Bacteria such as *Escherichia coli* (*E. coli*) use rotating helical flagella to swim. The body of *E. coli* is rod-shaped,

about 1 μm in diameter by 2 μm long, and, typically, has several flagella. Each flagellum has a rotary motor which can turn at approximately 100 Hz, either clockwise or counter clockwise. The motor is embedded in the cell wall, and drives a short flexible hook connected to the helical filament, which is about 20 nm in diameter and approximately 10 μm long (Berg 1993). Recently, Turner et al. (2000) succeeded in fluorescently labeling the filaments, allowing detailed visualization of the flagellar motion in real time. When all the flagella turn counterclockwise (when viewed from outside the cell body), they form a bundle that pushes the body forward in a run. When one or more of the motors reverses, the corresponding filaments unwind from the bundle, and the cell body moves erratically, or tumbles. Tumbles involve polymorphic transformations of the left-handed normal helices to the right-handed semi-coiled state, and then to the right-handed curly-1 state. The first transition reorients the cell body, and, once the motors reverse again, the curly-1 state transforms directly into the normal state, and the cell regains its initial speed once the complete bundle reforms (Turner et al. 2000). Tumbles and runs alternate, causing the cell to execute a three-dimensional random walk (Berg 1993). In the presence of a gradient of desirable chemicals (such as sugar), the cell reduces its likelihood of tumbling when it swims up the gradient, leading to a drift toward higher concentrations. The random motion of the cells may be exploited: it has recently been shown that a suspension of motile bacteria enhances fluid mixing in films (Wu and Libchaber 2000) and microchannels (Kim and Breuer 2004).

Because bacteria are so small, high-resolution microscopy methods are necessary for experimental studies. Direct visualization of the individual flagellar filaments in a rotating bundle is a daunting challenge, due to their 20-nm diameter. Also, micro-PIV approaches are currently incapable of resolving the flow pattern near the flagella, due to optical resolution and seeding limitations. To study the bundling process in more detail, Kim et al. (2003) developed a macro-scale model consisting of stepper-motor-driven polymer helices rotated in a high-viscosity silicone oil, and successfully simulated flagellar bundling for the counterclockwise rotation of left-handed helices (see also Jarosch 1989). By varying the motor speed and helix stiffness, they also showed that the motor period controls the initial rate of bundling. In this paper, we extend this work and use particle image velocimetry (PIV) to measure the flow induced by rotating helices. In Sect. 2, we describe our experimental setup. In Sect. 3, we present

Received: 12 November 2003 / Accepted: 24 June 2004
Published online: 20 October 2004
© Springer-Verlag 2004

M.J. Kim, M.J. Kim, J.C. Bird, T.R. Powers,
K.S. Breuer (✉)
Division of Engineering, Brown University, Providence,
RI02912, USA
E-mail: kbreuer@brown.edu

J. Park
Department of Mechanical Engineering, Ajou University,
443-749, Suwon, Gyeonggi(Republic of) Korea

It is a pleasure to acknowledge useful conversations with Howard Berg, Nick Darnton, Greg Huber, and Linda Turner. This work has been supported by the DARPA BioMolecular Motors Program and NSF grant no. CMS-0093658 (TRP). Some of the results in this paper were presented at the 5th international symposium on particle image velocimetry (PIV 2003), Busan, Korea, September 2003.

the results. First, we show that the PIV measurements of the flow induced by rigid rotating helices agree qualitatively with the predictions of slender-body theory. Then, we turn to flexible helices and present our main result: the rotational component of the flow due to the fully developed bundle is close to the flow generated by a single rotating rigid helix. Sect. 4 is the conclusion.

2 Experimental Setup

E. coli usually has several filaments per cell, but for simplicity, we consider the case with only two filaments. To accurately simulate the system at a more easily observable scale, the flagellar length was scaled up to approximately 10,000 times its normal value, resulting in flagella that were about 20 cm in length. Two series of experiments were performed. The first used rigid helices, made from copper tubing (4-mm diameter) bent around an aluminum mandril to match the shape of the full-scale flagella. The second series of measurements used flexible helices made from thin plastic tubing (4-mm diameter). The tubing was filled with epoxy to achieve the desired bending stiffness. To match the shape of the full-scale flagella, each flexible helix was wrapped around a cylindrical mandril during the curing process (Kim et al. 2003). The helical pitch (P) was 6.6 cm and the helix radius (R) was 1.27 cm. Reynolds number similarity was achieved (approximately) by rotating the helices at a low speed (about 0.25 Hz instead of 100 Hz) in high viscosity (100,000 cp) silicone oil (Polydimethylsiloxane). A second important non-dimensional parameter that must be preserved in the scale test is the ratio of viscous to elastic stresses, $M = \mu\omega L^4/EI$, where μ is the viscosity, ω is the rotation speed, L is the axial length of the helices, and EI is the bending stiffness. For bacteria, we estimate $M \approx 150$, while in our scale model, $M \approx 140$ for the flexible helices (Kim et al. 2003).

A pair of model flagella were placed into a rectangular tank (42×42×32 cm) of silicone oil and attached to a pair of synchronized stepper motors. Starting from a parallel position, they were rotated at the same speed. The rotation leads to flow, which, in the case of flexible helices, causes bundling for sufficiently large M (Kim et al. 2003). Black plates were also installed on the tank walls to minimize reflections from the laser flashes.

To measure the velocity, we seeded the oil with 23- μm -diameter silver-coated glass spheres (of density 1.6 g/cm³), and illuminated a plane in the tank with two pulses of a sheet of laser light in rapid succession. The velocity field was then computed using standard techniques (Raffel et al. 1998). We used chaotic mixing to disperse the tracer particles in the highly viscous silicone oil. The tank was mounted on a motorized turntable and rotated counter-clockwise (when viewed from above) at 3 rpm, while a fixed impeller with a nearly vertical shaft rotated clockwise (when viewed from above) at 33 rpm (Fountain et al. 2000). The anchor shape of the impeller was chosen for its suitability for mixing highly viscous liquids. From time to time, we manually varied the angle of the shaft of the impeller with the vertical from 0° to 20°. The primary difficulties were clumping of the powder of tracer particles and the slow rate of dispersion. To minimize clumping,

a small amount of tracer particles (5 g) was measured and uniformly scattered on the top of the silicone oil. Additional tracer particles were added periodically to the silicone oil until the volume fraction of the tracer particles reached 0.04%. It took 14 hours to complete the seeding of particles in the silicone oil tank.

The PIV system consisted of a Q-switched twin Nd:YAG laser (Quantel, Les Ulis Cedex, France), which provided frequency-doubled ($\lambda=532$ nm) pulsed emissions of up to 150 mJ/pulse, and a pulse duration of approximately 5 ns. The time delay Δt between the two successive pulses was chosen to be 10 ms. A combination of a cylindrical lens and a spherical lens collimated the laser light to a sheet of approximately 1-mm thickness at the measurement regions. Images were captured from two vantage points. In the first view, the laser sheet was aligned with the axes of the helices and images were taken from the front of the tank. In the second view, the laser sheet was perpendicular to the axes of the helices, and images were taken from below, via a mirror inclined at 45°. A full-frame interline-transfer 1,300×1,030×12-bit cooled CCD camera (IDT, Tallahassee, FL, USA) was used for recording the particle images. The CCD chip has an image plane measuring 8.7×6.9 mm (horizontal×vertical), and each pixel is square with side length $d_r=6.7$ μm . The field-of-view of PIV images was set as 165×130.7 mm ($l_x \times l_y$) for the flow measurement. A Nikon 24-mm manual lens with $f^\# = 2.8$ was attached to the CCD camera with magnification $M_o = 0.053$. Commercial software (IDT ProVision, Tallahassee, FL, USA) was used for the image recording, time synchronization control between the laser, and the CCD camera, and subsequent data processing. The velocity vectors were calculated using a 32×32-pixel interrogation window with adjacent windows overlapping by 50%.

The experimental uncertainties in the velocity field are determined by the accuracy of the measurement of particle displacements. The root-mean-square (rms) error in the velocity measurement is given by:

$$\sigma_u = \frac{\sigma_{\Delta x}}{M_o \Delta t} \quad (1)$$

where the image magnification $M_o = 0.053$ and $\sigma_{\Delta x}$ is the rms error of the displacement on the pixel plane. We take the rms error $\sigma_{\Delta x}$ to be 4% of the recorded image diameter (Adrian 1997):

$$\sigma_{\Delta x} = 0.04(d_e^2 + d_r^2)^{1/2} \quad (2)$$

where d_e is the optical diameter of the image prior to being recorded on the pixel plane, and $d_r = 6.7$ μm represents the resolution of the recording medium, and is taken to be equivalent to the pixel size. Assuming that the particle image is diffraction-limited and its image intensity is Gaussian, the diameter d_e of the diffracted particle image (Raffel et al. 1998), obeys the following:

$$d_e^2 = M_o^2 d_p^2 + [2.44(1 + M_o)f^\# \lambda]^2 \quad (3)$$

where, for the current case, the tracer particle diameter $d_p = 23$ μm , the f -number of the imaging lens $f^\# = 2.8$, and the laser wavelength $\lambda = 532$ nm. Thus, the recorded image diameter $(d_e^2 + d_r^2)^{1/2}$ is calculated to be 7.8 μm —a little

more than 1 pixel. Raffel et al. (1998) estimated an ideal particle image diameter, for minimum uncertainties, as ~ 1.5 pixels by using double-exposed PIV recording data. Substituting Eq. 3 into Eq. 2 gives $\sigma_{\Delta x} = 0.31 \mu\text{m}$, and, subsequently, the rms velocity measurement error as $\sigma_{u_i} = 0.59 \text{ mm/s}$. Thus, the minimum resolvable velocity fluctuation is acceptably small in comparison with the typical velocity of 1 cm/s . More accurate results would be possible with a greater time delay between pulses. However, this was not possible with the current synchronization system used at the time. In addition, the highly three-dimensional nature of the flow required a relatively short Δt so that the particles remained within the laser sheet between images.

3 Results and discussions

3.1 Validation

We tested our PIV system by measuring the flow induced by a cylinder with radius 12.7 mm , rotating at the center of the silicone oil tank. The analytic solution for the azimuthal velocity, v_θ , induced by a cylinder of radius R , rotating at the center of a circular tank of radius σR , is given by:

$$\frac{v_\theta}{\omega R} = \frac{1}{(\sigma^2 - 1)} \left[\frac{\sigma^2}{(r/R)} - (r/R) \right] \quad (4)$$

where ω is the rotational speed (Landau and Lifshitz 1987). Although the cross-section of our tank is square, not circular, the solution shown in Eq. 4 accounts for the effects of the walls accurately enough. Figure 1, shows a comparison of the analytic solution and the velocity

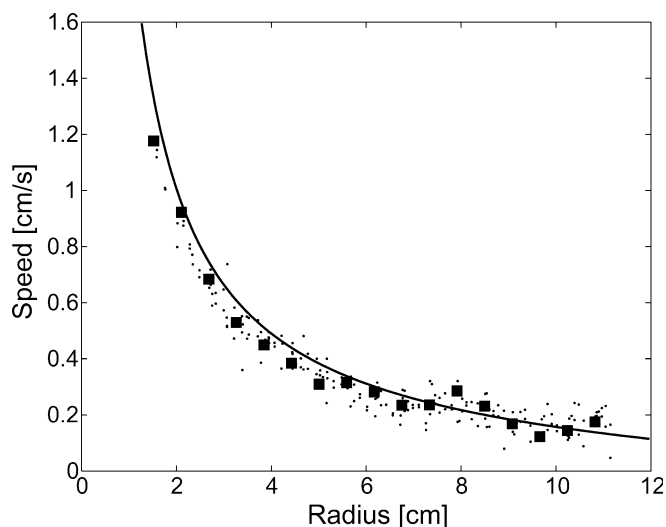


Fig. 1. Comparison between PIV measurements and analytical results for PIV validation. The *solid line* is the analytic solution for a cylinder of radius 12.7 mm rotating inside a concentric cylinder of radius 210 mm . The *symbols* are obtained from PIV measurements of the flow induced by a cylinder rotating in the square tank. The *small dots* are measurements taken at several radii, r , and angles, θ , while the *squares* are from measurements along a radial line with fixed θ

measured at several locations in the tank for $\omega = 0.2 \text{ Hz}$. The measured velocity field was confirmed to be rotationally symmetric, and very closely agreed with the analytic approximation given in Eq. 4 in the region near the cylinder ($R < r < 110 \text{ mm}$).

3.2 Rigid helices

The rigid helices were rotated at 0.25 Hz and image pairs were acquired at 2 Hz , resulting in eight velocity fields per rotation. Four cycles were recorded, and the resulting 32 velocity fields were checked for consistency position by position. Any vectors that statistically deviated from the others (typically due to a high error in the cross-correlation) were eliminated from the ensemble and then an average was taken over each interrogation window. In two regions of the flow—near the shadows of the helices and near the bright spots caused by reflected laser light from the surface of the helices—spatial averaging was used to smooth the velocity vectors.

For perfectly aligned rigid helices exactly in phase, the velocity fields should be periodic. Figure 2 shows the z components of four different instantaneous velocity fields, captured at the same phase angle, and viewed from below. The figure also shows a raw sample image and a sketch of the orientation of the laser sheet relative to the helices. Note the shadow cast by the helix, originating at the point at which the helix cuts through the laser sheet. The velocity fields are calculated using a standard cross-correlation technique without any type of vector validation or smoothing applied to the field. The velocity measurements in Fig. 3 are not identical and exhibit a standard deviation (averaged over the entire field) of 0.09 cm/s , compared to the maximum velocity of about 2 cm/s . However, the similarities between each realization are strong. The ensemble average of the four instantaneous velocity fields in Fig. 2 is shown in Fig. 3, and compared with results from a numerical slender-body calculation run at the same conditions and geometry (Kim and Powers 2004). The agreement is good, both quantitatively and qualitatively, except in the region where the shadow appears in the physical image and hinders the PIV processing. The PIV field shows a maximum velocity, which is about 9% smaller than that of the simulation. This discrepancy is slightly higher, but still comparable to that of the validation flow. In order to minimize the shadow effects on the PIV data, a larger interrogation cell (36×36 pixels) was needed in this region. In the case of flexible helices, the shadow effects were less severe since the flexible helices are translucent, and, thus, scatter less light than the solid copper helices.

Figure 4 shows a comparison between a PIV measurement and the corresponding numerical simulation for the vertical plane; the rotating speed is 0.25 Hz . This view shows the bands of positive and negative velocity generated by the helix pair rotation. Both figures show qualitative agreement in pattern. However, the velocity magnitudes are not quite matched between the simulation and the experiment. The maximum velocity in the side view PIV field is as much as 14% lower than the corresponding maximum in the simulation. The greater

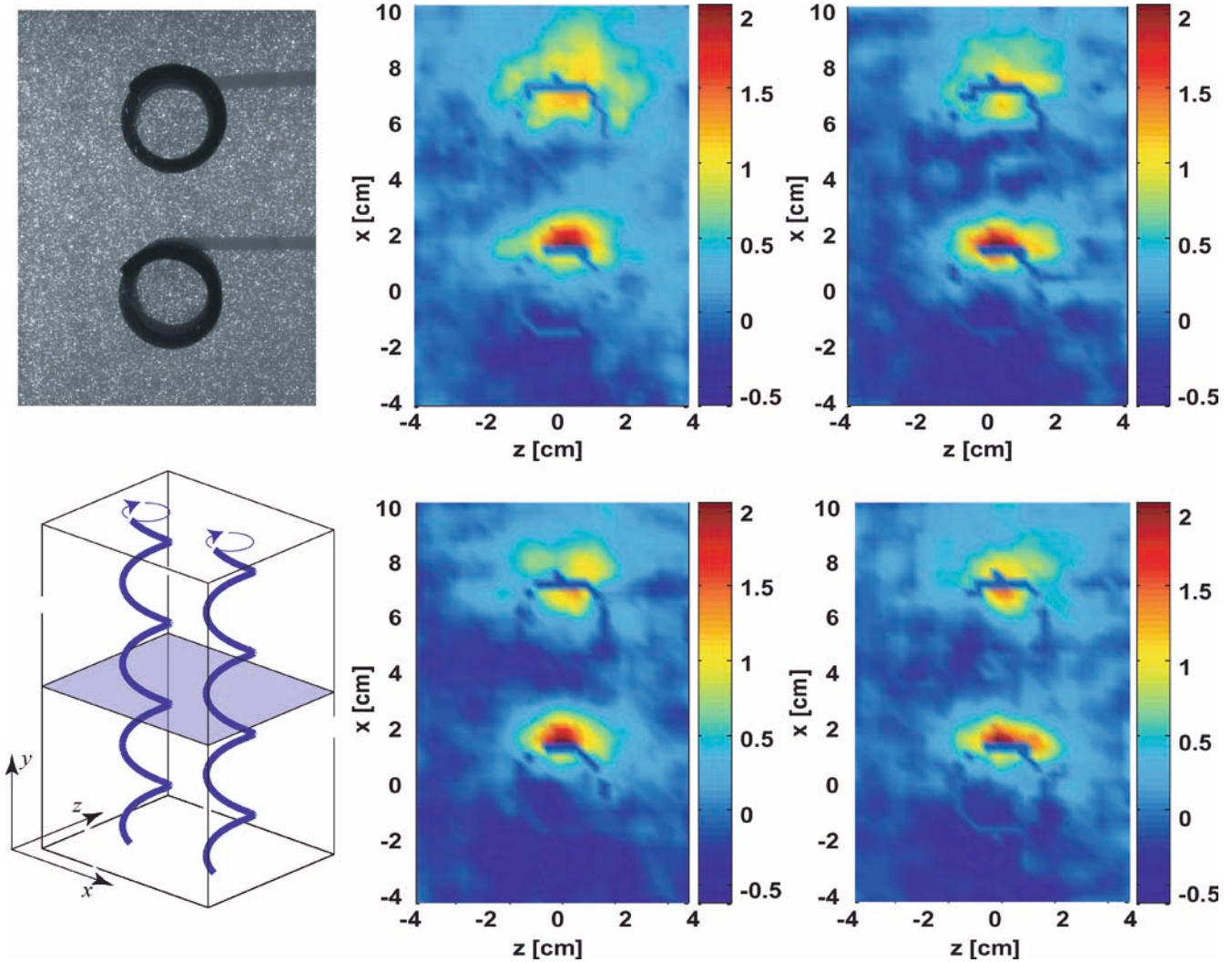


Fig. 2. PIV results of four separate measurements at the same periodic position for rigid helices rotating at 0.25 Hz. The view is looking up the helices towards the motors (which are at $y=4P$, where P is the helical pitch), and the color coding represents the z

component of velocity in cm/s in the plane at $y=2P$. Note that the helices can be discerned in the velocity field plots. The panels on the far left show the helices and tracer particles (*top*) and the sense of rotation and orientation of the light sheet (*bottom*)

discrepancy between experiment and simulation for the side view is expected because, in the side view, each helix pierces the sheet of light several times, leading to more shadows than the bottom view, where each helix only pierces the sheet of light once.

3.3

Flexible Helices

The flexible helices generate a more complex flow field since they deflect more and more as the experiment progresses. Furthermore, small changes in the initial orientation of the flagella mean that, although the overall characteristics of the flow and the bundling are quite similar, the flows are not exactly repeatable and, thus, ensemble averaging is impossible. However, ensemble results from the previous section indicate that the instantaneous flow field is a reliable measurement and that averaging does not significantly improve our understanding of the velocity field structure. Figure 5 shows the velocity field in the x - z plane (bottom view) during several stages of the bundling process. The

positions of the helices are clearly seen in the particle images (top panels) at three different times during the bundling. Since the motors run at a common constant velocity (0.25 Hz) and do not slip, the phase difference between the motor shafts is constant. When the motors turn counterclockwise, the helices rotate about each other, eventually entangling in a bundle, which persists indefinitely, as long as the motor speeds are sufficiently low.

The flow fields of Fig. 5 are complex and difficult to interpret. Furthermore, we cannot use numerical simulations as a guide to understanding the flow, since simulations for flexible helices are currently not available. However, we can use the PIV flows to answer a simple but important question: is the flow field of the fully developed steady-state bundle similar to the flow induced by a single rigid helix? To make a quantitative comparison, we averaged the azimuthal velocity (in the plane bisecting the two initial helix axes) over circles of constant radius, r , for the PIV measurements of the flow generated by the flexible helices, and for the slender-body theory simulation of the

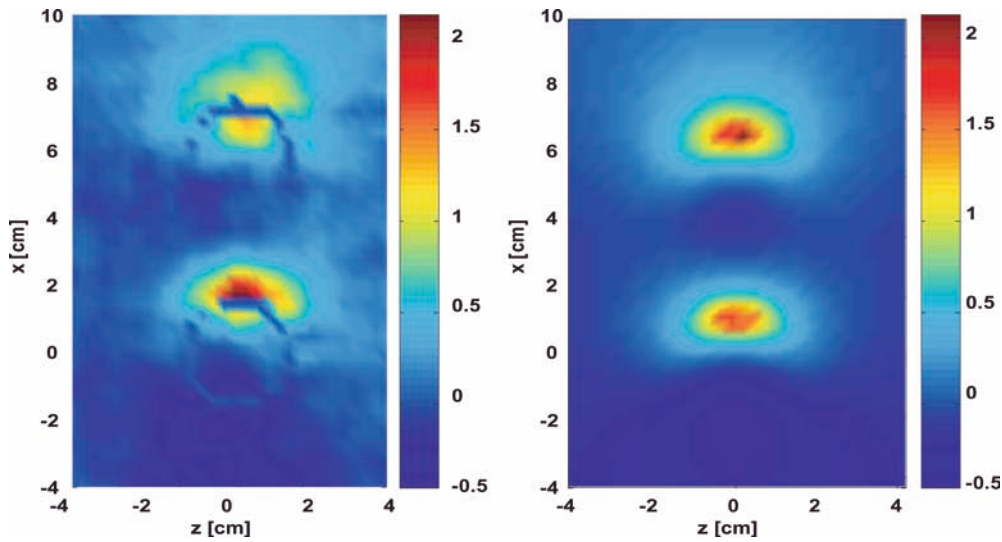


Fig. 3. Comparison of the z component of the velocity in the horizontal plane $y=2P$ measured by PIV (*left*) and computed numerically (*right*). The PIV results are the average of the four figures in Fig. 2. The units for the colored bars is cm/s

flow generated by a single rigid helix. We used helices with thicknesses of 4 mm and 8 mm in the simulations; the double thickness was chosen because, when the flexible helices entangle, the helix thickness is effectively doubled. Figure 6 shows the results and indicates excellent agreement between measurement and simulation. The lower of the two curves is the velocity due to a single rigid helix, and PIV data taken at two speeds is shown. The agreement is excellent both inside and outside the helix ring. There is some discrepancy in the immediate vicinity of the helix ring ($r/R=1$). PIV measurements in this region

are difficult due to reflections and shadows near the solid surface. In addition, the numerical simulation is also not completely reliable close to the solid surface, since the singular solutions of slender-body theory lead to diverging velocities at points just inside the surface. (Note that the lines drawn through the numerical results in Fig. 6 are to guide the eye; the sharp cusp at the maximum would be smoothed out if we calculated more points in this region.) Thus, the discrepancy is likely due to errors in both the theory and the measurement. The upper curve shows azimuthally averaged PIV data of the velocity due to a

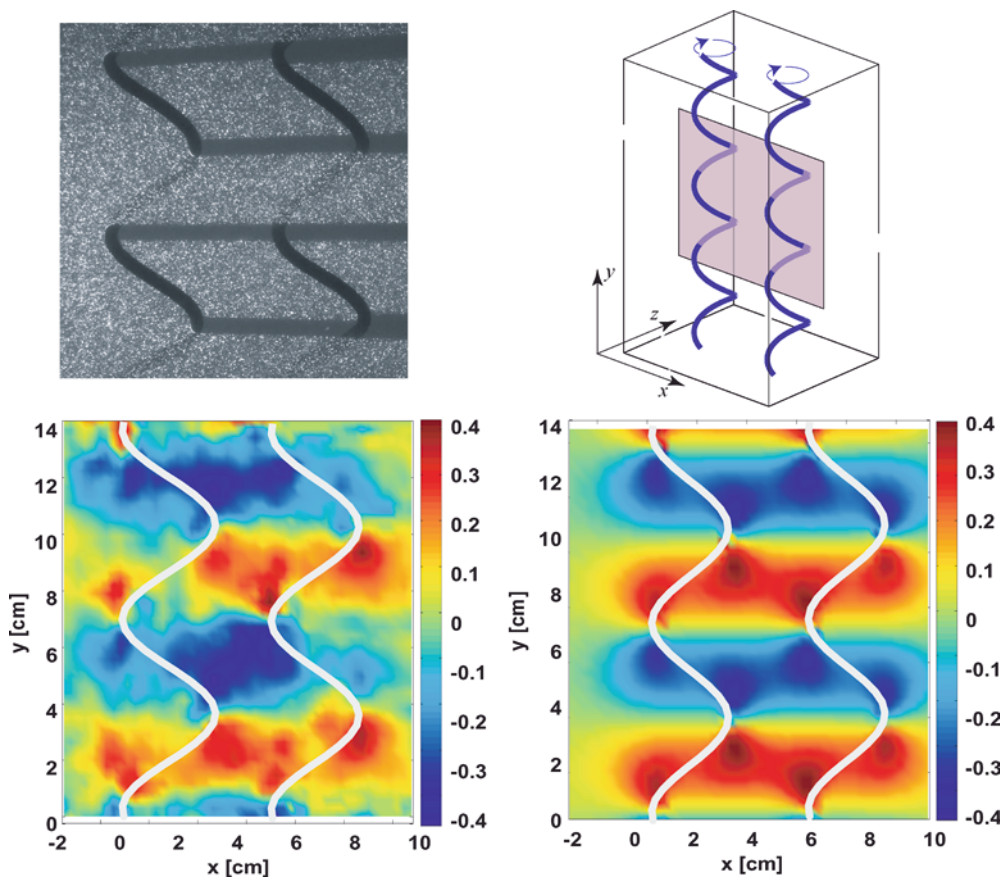


Fig. 4. Side view of flow induced by the rotation of two rigid helices. *Upper left*: raw image. *Upper right*: orientation of the sheet of laser light for the side view. *Lower left*: PIV measurement of the x component velocity when the rotation speed is 0.25 Hz. *Lower right*: corresponding numerical result. The units for the colored bars is cm/s

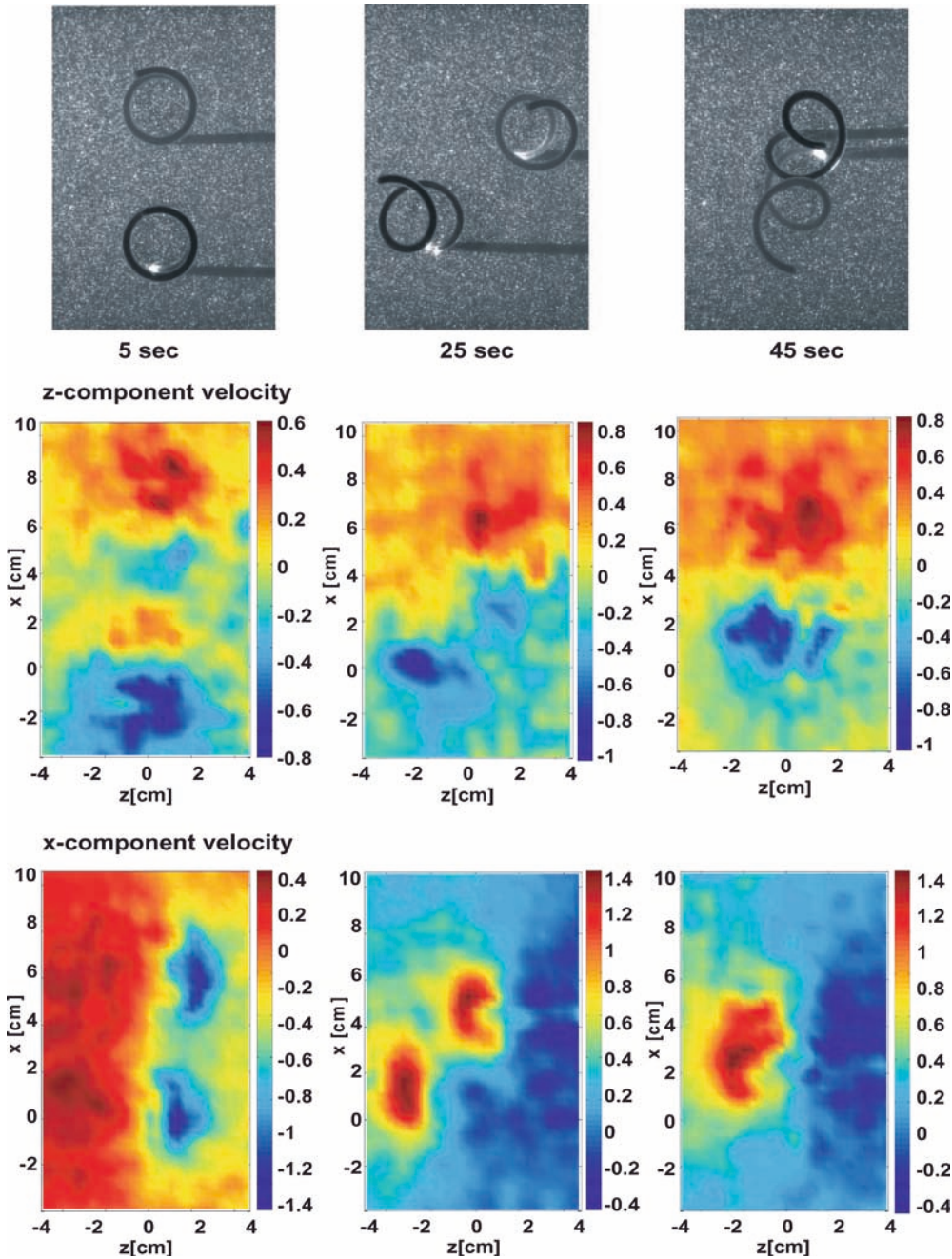


Fig. 5. Raw image and corresponding PIV measurements of velocity due to a bundling flexible helix pair ($y=2P$, rotated at 0.25 Hz) shown at 5 s (left), 25 s (middle), and 45 s (right) during the bundling process and viewed from below. The units for the colored bars is cm/s

helix bundle formed from two flexible helices (Fig. 6). These measurements are compared with the numerical solution of the flow due to a single rigid helix with a thickness double that of the baseline case (8 mm instead of 4 mm). As before, the agreement is remarkable, with the exception of the region near the helix body where the measurements indicate a lower and more smoothly varying velocity distribution to that predicted by the simulation.

The data suggest that the geometric complexities of the bundle do not contribute significantly to the overall flow, and that the flow of the steady-state two-helix bundle is, thus, closely approximated by the flow of a single rigid helix with twice the thickness. Note that there is a measurable difference between the flow in the

single-thickness and double-thickness simulations, indicating a weak but significant dependence of the flow on thickness. This dependence implies that, since our helices do not have exact geometric similarity to the full-scale flagella, there is a small but significant discrepancy between the model flows and the flagella-generated flows. Since the flow in slender-body theory depends logarithmically on the aspect ratio (see e.g. Kim and Powers (2004) and references therein), this discrepancy should get smaller as the aspect ratio of the model helix increases. However, for a given material, the bending stiffness of a helix decreases rapidly as the thickness decreases. Thus, faced with a compromise, we chose to match M accurately and the aspect ratio only roughly.

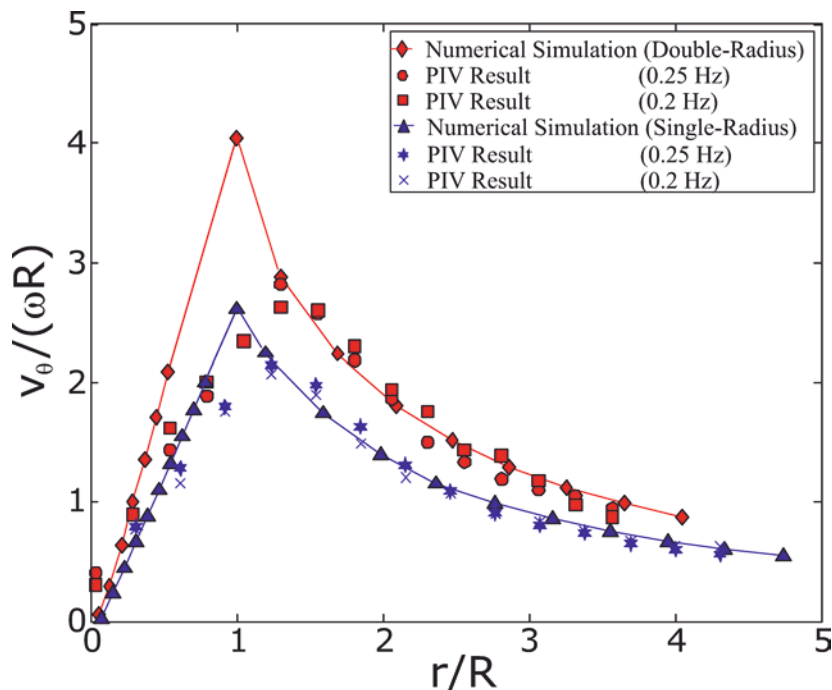


Fig. 6. Comparison between PIV measurements and slender-body calculations of the azimuthal velocity (averaged over a circle around the helix) as a function of the radius. Experimental results from two rotational speeds are shown, normalized by the angular speed ω , and helix radius, R . The PIV and numerical results in the lower curve are from the flow due to a single (rigid) helix of thickness 4 mm. The experimental data that form the upper curve are from the velocity, induced by a fully formed two-helix bundle, while the corresponding numerical solution corresponds to the flow due to the rotation of a single rigid helix with the thickness doubled (8 mm)

4

Conclusions

In this paper, we have presented PIV measurements of an extremely complex three-dimensional flow at a very low Reynolds number. The flow field is carefully constructed to match both the Reynolds number and the ratio of elastic and viscous stresses so that comparisons can be made with the flows generated by flagellated bacteria swimming through water at the micron scale. The velocity fields around rigid helices are compared with results from slender-body computations, and are found to agree qualitatively at the level of vector fields and quantitatively for the average azimuthal velocity, validating the technique. For the case of flexible helices, the deformation of the helices significantly complicates the flow field, and, since numerical computations, though feasible, have not yet been produced, no direct comparisons are possible. However, the measured rotational flow induced by the bundle in the steady state agrees well with calculated flow induced by a single rigid helix with twice the radius.

The highly three-dimensional nature of the flow also complicates the accuracy of the velocity measurements. The time separation between images was perhaps shorter than was desired for optimal PIV accuracy, but was restricted both by the specifics of the current synchronization system and by the need to keep particles inside the laser sheet between image pairs. These compromises likely added to the discrepancies between the measurements and their corresponding simulations. Nevertheless, these results do help considerably in our understanding of the microhydrodynamics of bacterial

motion, and we hope to extend them with fully three-dimensional PIV measurements in the future. In addition, we plan to take measurements over a wider range of values of M , and using a constant torque motor instead of the constant velocity motor used in the present work. Both of these extensions will aid in a more detailed understanding of the hydrodynamics of bacterial flagellar bundling.

References

- Adrian RJ (1997) Dynamic range of velocity and spatial resolution of particle image velocimetry. *Meas Sci Technol* 8:1393–1398
- Berg HC (1993) *Random walks in biology*. Princeton University Press, Princeton
- Fountain GO, Khakhar DV, Mezic I, Ottino JM (2000) Chaotic mixing in a bounded three-dimensional flow. *J Fluid Mech* 417:265–301
- Jarosh R (1989) Lateral hydrodynamic effects of rotating filaments. *Plant Syst Evol* 164(1–4):285–322
- Kim MJ, Breuer KS (2004) Enhanced Diffusion due to Motile Bacteria. *Phys Fluids* 16(9):78–81
- Kim MJ, Powers TR (2003) Hydrodynamics of rotating helices. *Phys Rev E* 69 061910 (2004)
- Kim MJ, Bird JC, Van Parys AJ, Breuer KS, Powers TR (2003) A macroscopic scale model of bacterial flagellar bundling. *Proc Natl Acad Sci USA* 100(26):15481–15485
- Landau LD, Lifshitz EM (1987) *Fluid mechanics*, 2nd edn. Pergamon Press, Oxford, England
- Raffel M, Willert C, Kompenhans J (1998) *Particle image velocimetry*, Springer, Berlin Heidelberg New York
- Turner L, Ryu WS, Berg HC (2000) Real-time imaging of fluorescent flagellar filaments. *J Bacteriol* 182:2793–2801
- Wu X-L, Libchaber A (2000) Particle diffusion in a quasi-two-dimensional bacterial bath. *Phys Rev Lett* 84:3017–3019